

## BASIC PARAMETER ESTIMATION OF BINARY NEUTRON STAR SYSTEMS BY THE ADVANCED LIGO/VIRGO NETWORK

CARL L. RODRIGUEZ<sup>1</sup>, BENJAMIN FARR<sup>1</sup> VIVIEN RAYMOND<sup>1,2</sup> WILL M. FARR<sup>1</sup> TYSON LITTENBERG<sup>1</sup> DIEGO FAZI<sup>1</sup> VICKY KALOGERA<sup>1</sup>

*Draft version May 28, 2013*

### ABSTRACT

Within the next five years, the Advanced LIGO/Virgo network will have reached a sensitivity sufficient to enable the routine detection of gravitational waves. Beyond the initial detection, the scientific promise of these instruments relies the parameter estimation techniques being currently developed. The majority of this effort has been towards the detection and characterization of gravitational waves from compact binary coalescence, i.e. the coalescence of black holes and/or neutron stars. While several previous studies have focused on the parameter estimation abilities of advanced detectors, the majority have relied on approximation techniques such as the Fisher Matrix. Here, we report the statistical uncertainties that will be achievable, in practice, using the parameter estimation techniques which will be applied to detections of binary neutron star systems. We find the recovery of the individual masses to be within fractionally within 10% at the 65% confidence level for equal-mass systems, and within 2% for unequal-mass systems. We also report the average uncertainties on the sky-locations, luminosity distance, and orbital inclinations of randomly distributed sources that can be achieved by different network configurations.

### 1. INTRODUCTION

By the end of the decade, the field of gravitational-wave astrophysics will mature into an ideal tool for exploring the gravitational side of the universe. Within the next few years, the first generation of gravitational-wave detectors capable of regularly resolving astrophysical sources will come online [CITE]. The Advanced LIGO and Virgo detectors will provide the first insights into the final moment of binary compact object mergers, including the merger of binary neutron star systems. Intense preparations are underway to characterize and extract as much physical information as possible from these signals.

The mergers of binary neutron stars are expected to be the most common source in the advanced detector era [CITE]. Models from stellar evolution suggest that the number of binary neutron star mergers within Advanced LIGO/Virgo's detection horizon could reach into the hundreds per year [CITE]. Although the peak sensitivity of ground-based detectors is not focused on the frequency at which BNS systems merge, it could still be possible to extract information about both strong field gravitational physics [CITE] and the hydrodynamics of dense matter (e.g. the equation of state of nuclear matter) [CITE]. Furthermore, the observations of multiple BNS systems will provide key insight into the evolution of binary systems in the field [CITE], and in globular clusters [CITE]. As such, BNS systems will likely form the “bread and butter” of the compact binary coalescence detection effort in the coming years.

Of course one must distinguish between the detection of such events, and the precision measurement of the relevant

physical parameters. The detection of BNS systems will be performed with a matched filtering approach. By comparing the data stream with a bank of theoretical templates, the time-series data can be searched for candidate signals at a sufficiently rapid rate to analyze months of data. When the overlap between one of the template waveforms and the detector output is sufficiently large (97%), a detection candidate is found. However, the parameter space of these signals can be highly degenerate, with several locations in parameter space corresponding to nearly identical waveforms. In order to fully realize the science potential of these instruments, we must perform a full exploration of the parameter space for each detection. By analyzing the parameter space of each candidate with a Bayesian inference technique we will be able to make precise, scientifically meaningful statements about the physics of these detectable systems. To that end, we employ a Markov-Chain Monte Carlo sampling algorithm, `lalinference_mcmc`, included in the LIGO Application Library parameter estimation code, `LALInference`, to analyze the parameter space of binary neutron star systems.

By employing the full parameter-estimation machinery that will eventually be used in the Advanced LIGO/Virgo era, our results give the first estimate at the realistic capabilities of advanced ground-based detectors to characterize BNS systems. Until recently, the majority of studies have employed the Fisher matrix formalism which was first adapted for gravitational-wave parameter estimation by (Finn 1992). While each of these studies (Poisson & Will (1995); Cutler & Flanagan (1994); Arun et al. (2005), among many others) have pointed out the limitations and flaws of the Fisher Information Matrix, there has been no study which investigates the BNS parameter estimation capabilities of Advanced LIGO/Virgo via the techniques that will eventually be employed. The recent work of Vallisneri (2008) and our own work (Ro-

<sup>1</sup> Center for Interdisciplinary Exploration and Research in Astrophysics (CIERA) & Dept. of Physics and Astronomy, Northwestern University, 2145 Sheridan Rd, Evanston, IL 60208, USA; [e-mail: [cr@u.northwestern.edu](mailto:cr@u.northwestern.edu)]

<sup>2</sup> California Institute of Technology, Pasadena, CA 92215, USA

driguez et al. 2013) has demonstrated that the Fisher matrix cannot even be treated as a lower bound on the standard deviations of certain parameters (particularly the masses) measurable in gravitational-wave detectors.

In this paper, we perform a systematic study of the statistical uncertainties with which the Advanced LIGO/Virgo network will be able to measure the basic parameters of binary neutron stars. In Section 2, we describe the machinery of our parameter estimation code, `LALInference`, and the associated MCMC sampler, `lalinference_mcmc`, as well as the frequency-domain gravitational-wave template we employ. In Section 3, we qualitatively analyze the posterior probability density functions for BNS systems with different masses and extrinsic parameters. The results are divided into three parameter sets of interest: the recovery of the mass parameters (Section 3.1), the recovery of the orbital inclination and luminosity distance (Section 3.2), and the localization of sources in the sky (Section 3.3). Finally we provide quantitative 1-dimensional confidence intervals on the parameter recovery in Section 4. These results, contained in Tables 1 and 2, are intended as a reference for the optimal BNS parameter estimation capabilities of Advanced LIGO/Virgo. We assume that  $G = c = 1$  throughout.

## 2. PARAMETER ESTIMATION

We begin by introducing a Bayesian formalism for parameter estimation. We assume that the time-domain signal in a gravitational-wave network can be written as a combination of a gravitational waveform  $h_0$  and the noise of the detector  $n$ . We further assume that this noise is stationary and Gaussian with zero mean. Therefore, the detector output is simply

$$s = n + h_0. \quad (1)$$

Since our noise model is Gaussian, we can write the probability of a specific signal realization  $s$  as proportional to the probability that our residual is Gaussian distributed once the waveform has been subtracted

$$\begin{aligned} p(s|\boldsymbol{\theta}) &\propto \exp\left[-\frac{1}{2}\langle n|n\rangle\right] \\ &= \exp\left[-\frac{1}{2}\langle s - h(\boldsymbol{\theta})|s - h(\boldsymbol{\theta})\rangle\right], \end{aligned} \quad (2)$$

where  $\boldsymbol{\theta}$  is the set of parameters for our template waveforms, and  $p(s|\boldsymbol{\theta})$  is the likelihood of the signal  $s$  given the parameters  $\boldsymbol{\theta}$ . The inner product,  $\langle | \rangle$ , is defined using the noise spectrum of the detectors as

$$\langle a|b\rangle \equiv 4\Re \int \frac{\tilde{a}(f)\tilde{b}^*(f)}{S_n(f)} df, \quad (3)$$

where  $S_n(f)$  is the one-sided power spectral density as a function of frequency, and  $\tilde{a}(f)$  and  $\tilde{b}(f)$  are the Fourier transforms of the time-domain signals  $a(t)$  and  $b(t)$ .

Once we have the likelihood of the signal (2), we employ Bayes Theorem to obtain the posterior probability

of the system parameters  $\boldsymbol{\theta}$  given the signal  $s$  as

$$\begin{aligned} p(\boldsymbol{\theta}|s) &= \frac{p(\boldsymbol{\theta})p(s|\boldsymbol{\theta})}{p(s)} \\ &\propto p(\boldsymbol{\theta}) \exp\left[-\frac{1}{2}\langle s - h(\boldsymbol{\theta})|s - h(\boldsymbol{\theta})\rangle\right], \end{aligned} \quad (4)$$

where  $p(\boldsymbol{\theta})$  are the prior probabilities on our source parameters and  $p(s)$  is a normalization constant.

We are interested in the posterior  $p(\boldsymbol{\theta}|s)$  as it encodes information about prior state of knowledge about the problem. For instance, since it is assumed that compact binaries form homogeneously in the local universe, we can safely assume that the population of sources will be distributed homogeneously in volume, or evenly in  $D^2$ . Our prior information can come from mathematical limits in the parameter space or from our *a priori* knowledge of astrophysical systems. We employ priors which are

- uniform in component masses from  $0.8M_{\odot} \leq M_{1,2} \leq 30M_{\odot}$ , with a minimum chirp mass (7) of  $0.6M_{\odot}$ ,
- uniform in volume, which implies a luminosity distance prior of  $p(D) = D^2 dD$ , and
- uniform in all other parameters.

If we pick a set of parameters  $\boldsymbol{\theta}$  such that  $h(\boldsymbol{\theta}) = h_0$ , then the posterior (4) will be near a global maximum; however, the presence of noise will in general deflect the maximum of our posterior away from the value at  $\boldsymbol{\theta}_0$ . That is, in the presence of noise, there is no guarantee that the maximum-likelihood of our signal corresponds to the true parameters of the system.

### 2.1. Markov-Chain Monte Carlo

The LIGO Algorithm Library parameter estimation code, `LALInference`, is designed as a unified framework for gravitational-wave parameter estimation. By using a common setup for waveform generation, PSD estimation, data handling, and other associated techniques from gravitational-wave parameter estimation, `LALInference` allows the implementation of multiple parameter samplers in using identical parameter setups, including Nested Sampling (`lalinference_nest`) [CITE] and Markov-Chain Monte Carlo (`lalinference_mcmc`). We elect to use the MCMC sampler for this study. `lalinference_mcmc` is based upon the previously described code, `SpinSpiral` (van der Sluys et al. 2009; Raymond et al. 2010). The MCMC employs a Metropolis-Hastings sampling algorithm, which can be described as follows (Gilks 1999):

1. Pick an initial point in the parameter space ( $\boldsymbol{\theta}_{\text{old}}$ ), and then propose a random “jump” to a new set of waveform parameters,  $\boldsymbol{\theta}_{\text{new}}$ . The jump follows the (conditional) probability distribution  $q(\boldsymbol{\theta}_{\text{new}}|\boldsymbol{\theta}_{\text{old}})$ .
2. Calculate the posterior probability,  $p(\boldsymbol{\theta}_{\text{new}}|s)$ , of the new parameters using (2) and (4).
3. Accept the new parameters with probability

$$p_{\text{accept}} = \min\left[1, \frac{p(\boldsymbol{\theta}_{\text{new}}|s)q(\boldsymbol{\theta}_{\text{old}}|\boldsymbol{\theta}_{\text{new}})}{p(\boldsymbol{\theta}_{\text{old}}|s)q(\boldsymbol{\theta}_{\text{new}}|\boldsymbol{\theta}_{\text{old}})}\right]. \quad (5)$$

If the new parameters are accepted, record  $\boldsymbol{\theta}_{\text{new}}$  and repeat with  $\boldsymbol{\theta}_{\text{old}} \leftarrow \boldsymbol{\theta}_{\text{new}}$ ; otherwise, record  $\boldsymbol{\theta}_{\text{old}}$ , and repeat.

The above procedure is designed to record a chain of samples whose distribution is  $p(\boldsymbol{\theta}|s)$ . By drawing a sufficient ( $\sim 1000$ ) number of effective samples from the posterior, the chains traces out the functional form of the posterior, gathering more samples from regions with high posterior probability. Depending on the proposal distribution,  $q$ , the convergence (mixing) of the chain may be rapid or slow. We employ multiple optimization techniques, including both specially-crafted  $q$  and parallel tempering, to ensure adequate mixing of the Markov Chains throughout our parameter space. The details of the algorithm can be found in (van der Sluys et al. 2008, 2009; Raymond et al. 2010). Both samplers were tuned and developed during the last science run of the Initial LIGO/Virgo network. A description of the parameter estimation capabilities of these two samplers with respect to real gravitational-wave data, as well as a more detailed description of the algorithms and checks for convergence, can be found in the LIGO Scientific Collaboration et al. (2013).

## 2.2. Waveform Model

We use a frequency domain waveform accurate up to 3.5 post-Newtonian (pN) order in phase and amplitude. We restrict ourselves to quasi-circular, non-spinning waveforms as a simplifying assumption. The standard form of our waveform model, known as the *TaylorF2* approximant, is calculated via the stationary-phase approximation. In this setup, the gravitational-wave amplitude is given by

$$\tilde{h}(f) = a(t_f)e^{i\psi(f)}, \quad (6)$$

where  $a(t_f)$  is the amplitude evaluated at a stationary-phase reference point, which to lowest order takes the form  $A \propto f^{-7/6}\mathcal{M}_c^{5/6}\Theta(\text{angle})/D$ ,  $D$  is the luminosity distance of the binary, and  $\psi(f)$  is the pN phase.  $\Theta(\text{angle})$  is a function of the orbital orientation with respect to the detector network in terms of the sky position, orbital inclination, and the wave polarization. In addition to the total mass,  $M_{\text{tot}} \equiv M_1 + M_2$ , it is convenient to work with the *mass ratio* and *chirp mass*, defined by

$$q \equiv M_1/M_2 \quad \text{and} \quad \mathcal{M}_c = (M_1 M_2)^{3/5} M^{-1/5}, \quad (7)$$

respectively.<sup>3</sup> The stationary phase then becomes an expansion in the Newtonian orbital velocity,  $v = (\pi M f)^{1/3}$ ,

$$\psi(f) = 2\pi f t_c - \phi_0 + \frac{\pi}{4} + \frac{3}{128} \left( \frac{M}{\mathcal{M}_c} \right)^{5/3} \sum_{k=0}^n \alpha_k v^{k-5} \quad (8)$$

where the  $\alpha_k$  coefficients are taken from the pN expansion to order  $n/2$ . See Buonanno et al. (2009) for a description and comparison of different waveform families.

<sup>3</sup> Most gravitational-wave literature instead uses the *symmetric mass ratio*, defined as  $\eta \equiv M_1 M_2 / M^2$ . We elect to use  $q$  as it is more physically intuitive, and the prior  $p(q)$  is uniform when the component mass priors are uniform.

The terms  $t_c$  and  $\phi_0$  in equation (8) are constants of integration, referred to as the chirp time and coalescence phase, respectively.

To perform the integral defined in (3), we used as our power-spectral density the best estimate for a high-power, zero-detuning configuration of Advanced LIGO, provided by the LIGO Scientific Collaboration. Both the noise curve and technical reports describing it can be found in Shoemaker (2009). We consider two configurations of the advanced detector network: a three-detector configuration consisting of the two LIGO sites (in Hanford, WA and Livingston, LA) and the Virgo site (in Pisa, Italy), and a four-detector configuration with adds the proposed LIGO-India detector (in Chitradurga, KA). For simplicity, we assume each detector to be operating at the Advanced LIGO sensitivity.

For a multi-detector network, the noise-weighted inner products (3) combine linearly, allowing us to use the above formalism with minimal modification. We integrate the inner product from a lower-frequency cutoff of 20Hz to the innermost-stable-circular orbit of the systems in question, which for a non-spinning binary is a function only of the total mass:

$$\pi f_{\text{ISCO}} = \frac{1}{6^{3/2} M}. \quad (9)$$

We consider the mass parameters  $(\mathcal{M}_c, q)$  and the phasing parameters,  $(\phi_0, t_c)$ , to be the intrinsic parameters of a gravitational-wave signal. There are an additional 5 extrinsic parameters, independent of the pN orbital phase, which can modulate the amplitude of the signal in an independent fashion for each detector. Combining these leads to our 9-dimensional parameter space for non-spinning systems:

$$\boldsymbol{\theta} = (\mathcal{M}_c, q, \phi_0, t_c, D, \iota, \psi, \alpha, \delta) \quad (10)$$

where to summarize

- $\mathcal{M}_c$  is the chirp mass,
- $q$  is the mass ratio,
- $\phi_0$  and  $t_c$  are the chirp phase and chirp time, arbitrary phasing parameters,
- $D$  is the luminosity distance to the binary,
- $\iota$  is the orbital inclination,
- $\psi$  the gravitational-wave polarization, and
- $\alpha$  and  $\delta$  the right ascension and declination of the source on the sky.

Since the wave amplitude depends on the orientation of the binary with respect to each detector, most of the information about these extrinsic parameters comes from two sources: the time-of-arrival triangulation of the source locations, and the relative amplitudes within the detector network.

We define the signal-to-noise ratio (SNR) of a gravitational wave in a single detector as

$$\rho \equiv \frac{4}{\sigma} \int_0^\infty \frac{|\tilde{s}(f)\tilde{h}(f)|}{S_n(f)} df \quad (11)$$

where  $\rho$  is the SNR and  $\tilde{s}(f)$  and  $\tilde{h}^*(f)$  are the frequency-domain signal and template, respectively, and the normalization  $\sigma$  is given by

$$\sigma^2 = 4 \int_0^\infty \frac{|\tilde{h}(f)|^2}{S_n(f)} df. \quad (12)$$

When dealing with network of gravitational-wave detectors, the SNRs of the individual detectors add in quadrature. That is, the network SNR for a detection is

$$\rho_{\text{network}} = \sqrt{\sum_i \rho_i^2} \quad (13)$$

where  $\rho_i$  is the SNR, given by (11), of the  $i^{\text{th}}$  detector.

For this study, we consider four separate populations of BNS systems, with component mass combinations of  $1M_\odot/1M_\odot$ ,  $1.4M_\odot/1.4M_\odot$ ,  $1M_\odot/2.5M_\odot$ , and  $2.5M_\odot/2.5M_\odot$ . Each population consisted of 40 signals distributed randomly in sky location, polarization, inclination, time-of-arrival, and coalescence phase. The luminosity distance,  $D$ , was selected to provide a network SNR of  $\rho_{\text{network}} = 20$  for each source. While unphysical from an astrophysical perspective (binary sources should be distributed evenly in comoving volume), this choice allows us to explore the parameter estimation in the context of optimal detection candidates.

Finally, note that the power-spectral density that defines the inner product (3) is simply the time-averaged sensitivity of a given detector to a specific frequency. Ignoring non-Gaussian glitches, any stretch of data should contain a specific noise realization drawn from a Gaussian colored by the PSD. However, what we are interested in is not the parameter estimation that can occur in a specific draw from this probability of noises, but the uncertainties averaged over all possible noise realizations.<sup>4</sup> Since our noise model is assumed to be Gaussian, it is unnecessary to recover the parameters from a large sample of identical waveforms in different noise; we can simply assume the noise is the mean defined by the power-spectral density. This “zero-noise” parameter estimation provides a statistical statement on the measurable uncertainties, and is what is reported here. In Section 3.4 we provide an example of parameter estimation in several non-zero noise realizations compared to the zero-noise equivalent [TYSON WILL WRITE].

### 3. RESULTS

Of the nine parameters in the domain of the waveform, only six are particularly physically interesting: the masses of the two binaries,  $M_1$  and  $M_2$ , the orbital inclination,  $\iota$ , the angular position on the sky,  $\alpha$  and  $\delta$ , and the luminosity distance of the source,  $D$ . While the coalescence phase  $\phi_c$ , the coalescence time  $t_c$ , and the wave polarization  $\psi$  must be included in any parameter estimation of the waveform, they do not encode any information of particular astrophysical interest.<sup>5</sup>

<sup>4</sup> Similarly to how the Fisher matrix formalism can provide the Cramer-Rao bound averaged over all noise realizations

<sup>5</sup> For systems whose components are non-spinning. The presence of intrinsic angular momentum will, in general, couple to the coalescence phase and wave polarization.

In Figure 1, we provide an example of the nine, 1-dimensional marginalized posterior probability density functions recovered from a single  $1.4M_\odot/1.4M_\odot$  BNS system. These PDFs are the typical of the type of results that will be produced by parameter estimation studies in the advanced detector era. Notice that the peak of several parameters, including the chirp mass,  $\mathcal{M}_c$ , appears to be displaced from the true values in red. This effect is due to the reduction of the 9-dimensional PDF to a series of marginalized 1-dimensional PDFs. For instance, the 1-dimensional PDF for chirp mass is marginalized via

$$p(\mathcal{M}_c|s) = \int_{\boldsymbol{\theta} \setminus \mathcal{M}_c} p(\boldsymbol{\theta}|s) d(\boldsymbol{\theta} \setminus \mathcal{M}_c) \quad (14)$$

where the notation  $\boldsymbol{\theta} \setminus \mathcal{M}_c$  implies all parameter of (10) except  $\mathcal{M}_c$ . Other parameter and higher-dimensional marginalizations follow a similar convention. In practice, the MCMC samples make this integral trivial: since the samples are distributed according to the posterior, (14) can be calculated by simply reading off the relevant samples in a single parameter, implicitly calculating a Monte-Carlo integral over all other parameters.

#### 3.1. Mass Parameters

Of the nine variables in our parameter space (10), the two of immediate physical interest are the two parameters,  $\mathcal{M}_c$  and  $q$ , or correspondingly the direct masses of the two companions,  $M_1$  and  $M_2$ . As stated above, the ability of Advanced LIGO/Virgo to construct a population of BNS masses will be one of the more useful applications of gravitational-wave astronomy.

We find that there is virtually no difference between the mass PDFs of our different injected signals within each mass bin. While this may initially seem disconcerting, it is to be expected. Recall that of the BNS signals were injected with a network SNR of 20 into a zero-noise detector realization. Furthermore, note that the mass parameters are the only two which directly effect the phase of the TaylorF2 waveform (8). Therefore, as long as the injected mass parameters are identical within each mass system, and as long as the injected SNR is identical, the amount of recoverable information in each mass parameter should be almost identical, and for a sufficiently converged MCMC chain, the recovered posterior PDF should be identical.

This effect can be summarized as follows: for non-spinning systems, the posterior probability of the masses,  $p(\mathcal{M}_c, q|s)$ , does not depend strongly on the recovery of the extrinsic parameters,  $\phi_0$  or  $t_c$ . Therefore, systems with identical masses will produce identical mass PDFs. The only noticeable difference will come from the specific realization of noise produced by the detector, which we address in Section 3.4.

In Figures 2 and 3, we show the marginalized 2D posterior PDFs of our mass parameters for prototypical equal mass and unequal mass binaries. We include the PDF in both the  $\mathcal{M}_c$ - $q$  space (relevant for the waveform and the MCMC algorithm), and the more physically interesting component mass space ( $M_1$ - $M_2$ ). Although only the  $1.4M_\odot/1.4M_\odot$  system is included in Figure 2, the PDF is quantitatively identical to the other equal mass cases, modulo a scaling factor.

## Example 1D Posterior Probability Densities for $1.4M_{\odot}/1.4M_{\odot}$ System

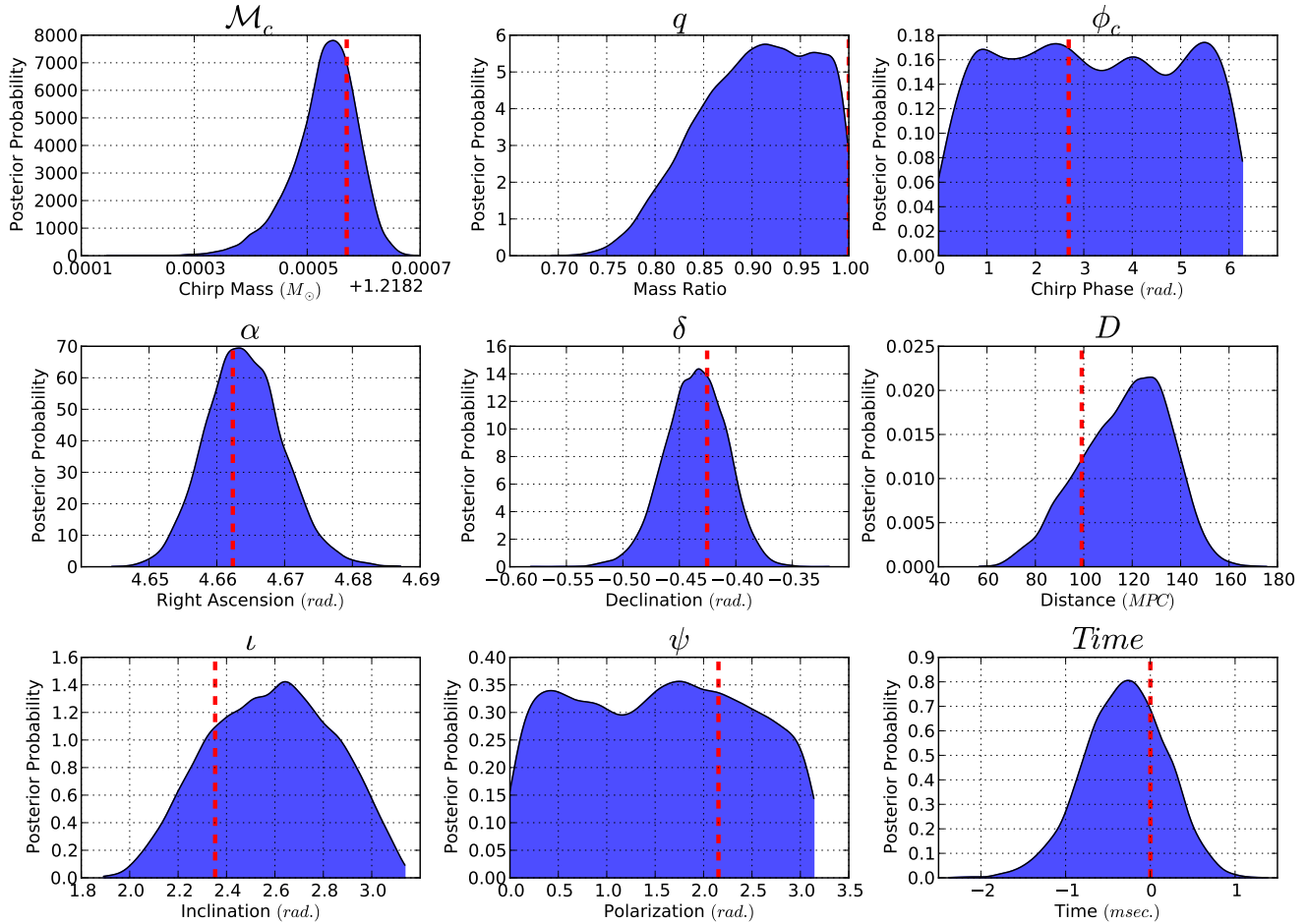


FIG. 1.— Marginalized 1D posterior probability density functions taken from a typical  $1.4M_{\odot}/1.4M_{\odot}$  BNS system. We have plotted each of the 9 parameters for our non-spinning BNS problem as stated in section 2.2. Note how, even for parameters with excellent recovery, the peak of the 1D Gaussian is displaced from the injected value (in dashed red). This is not due to a systematic bias, but is caused by the marginalization of a single dimension from the full 9D posterior space. To better see this effect, compare the 1D PDF for  $\mathcal{M}_c$  and  $q$  with the 2D marginalized PDF in Figure

To condense the results into a single figure of merit, we average the 1-dimensional mass PDFs into a single posterior probability for system. See Figure 4. Notice how when averaged and normalized to the injected values, the recovery of the component masses depends only on the mass ratio. Furthermore, for systems of equal masses, the posterior barely extends beyond 15% of the injected values. If one assumes that the threshold between black holes and neutron stars lies at approximately  $3M_{\odot}$ , then it might be assumed that the mass recovery would allow one to discriminate between black holes and neutron stars.

Unfortunately, this will not be feasible in practice. We have neglected the spin of the binaries, which will be highly correlated to the masses. This coupling means that a higher-massed spinning black hole systems can produce waveforms very similar to non-spinning, low-mass, making it impossible to discern between non-spinning neutron stars and spinning, more massive black holes. However, the situation is not hopeless: if the spins

are misaligned, the spin vectors will couple to the orientation of the binary (encoded in the three angles  $\phi_0$ ,  $\iota$ , and  $\psi$ ) via relativistic precession. It remains to be seen if using fully spinning waveforms will make it possible for Advanced LIGO/Virgo to discern binary neutron stars from their spinning black hole counterparts.

In Table 1, we list the 65% fractional confidence intervals for the mass parameters. We find that the component masses for equal mass systems can be isolated to between 6% and 9% fractional uncertainty at the 65% confidence interval. This value drops to less than 2% for the components of the unequal mass systems. Again, this neglects the effects of spin which can substantially increase these values.

### 3.2. Inclination and Distance

Binary neutron star systems (along with neutron star/black hole systems) are one of the best candidates for progenitors of short-hard gamma-ray bursts (Nakar 2007, and references therein). After merger, the remnant

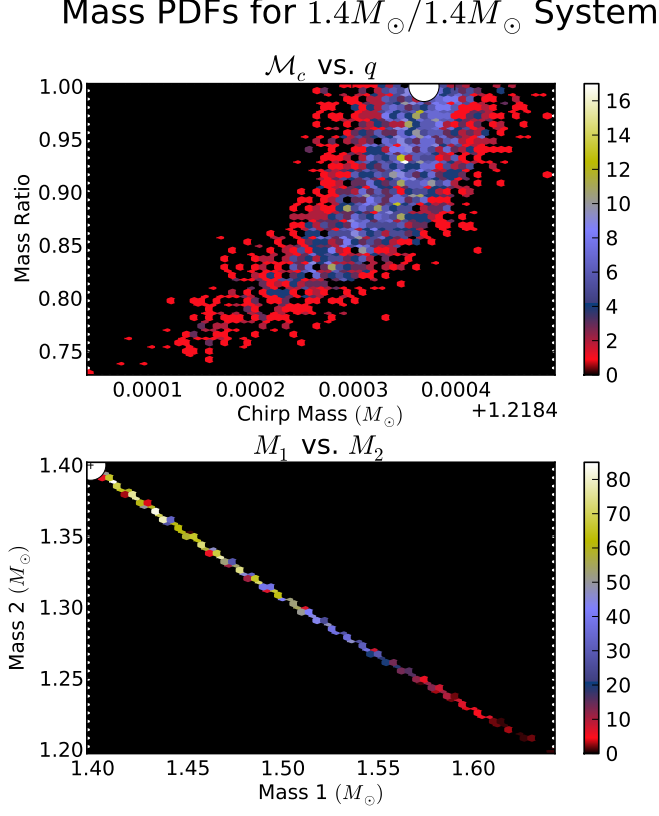


FIG. 2.— 2D marginalized posterior probability density functions for the mass parameters recovered in typical a  $1.4M_{\odot}/1.4M_{\odot}$  system. The posteriors are plotted in terms of parameters used in the waveform, chirp mass ( $\mathcal{M}_C$ ) and the mass ratio ( $q$ ), and in the individual component masses of the binary ( $M_1$  and  $M_2$ ). In the  $\mathcal{M}_c$ - $q$  space, the posterior would resemble a Gaussian if not for the limitation of  $q \leq 1$ . The presence of the  $q$  cutoff and the convention that  $M_1 \geq M_2$  inform the non-Gaussian features present. When projected as 1D marginalized posteriors, the component masses resemble the posterior PDFs shown in figure 4.

is believed to emit the burst along the axis of orbital angular momentum, making the inclination of the binary system of particular interest to gamma-ray astronomy (Abadie et al. 2010; Corsi et al. 2012). The inclination is detected as a relative amplitude difference between the two gravitational-wave polarization, such that to lowest order

$$\begin{aligned} h_+(f) &= \frac{1 + \cos^2(\iota)}{2D} \tilde{h}(f) \\ h_{\times}(f) &= i \frac{\cos(\iota)}{D} \tilde{h}(f) \end{aligned} \quad (15)$$

It should be apparent that the luminosity distance  $D$  and the inclination  $\iota$  can be highly correlated in any parameter estimation study.

Given this degeneracy, it should come as no surprise that the 2D marginalized posteriors of distance and inclination are the worst of the six physically interesting parameters. Four typical 2D PDFs are presented in Figure 5. Notice the bimodal uncertainty present in the top 2D PDF along the  $\iota$  axis, due to the similarity between the evaluated likelihoods at  $\iota$  and  $\iota + \pi/2$ . As the majority of the information extracted via parameter estimation

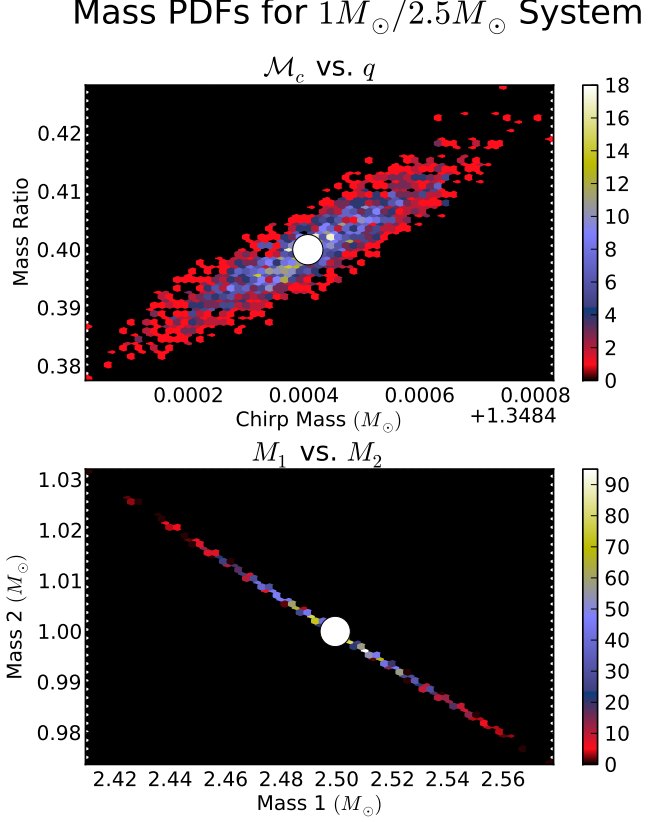


FIG. 3.— Similar to Figure 2, for a typical  $1M_{\odot}/2.5M_{\odot}$  system. The unequal mass ratio displaces the posterior PDFs from the  $q \leq 1$  present in the equal mass case, yielding a Gaussian PDF in both the  $\mathcal{M}_c$ - $q$  and  $M_1$ - $M_2$  spaces.

is from the phase of the signal, the recovery of a posterior in  $D$ - $\iota$  space will be limited, even during the Advanced LIGO/Virgo era; however, there will be cases (such as the first PDF in Figure 5) that will prove copacetic to simultaneous measurements accurate enough for coincidence measurements with GRB observers. Conversely, if a gravitational-wave signal is matched to a detected GRB counterpart, the optical information about the orbital inclination will provide an additional constraint on the  $D$ - $\iota$  space to vastly improve the results quoted here.

In Table 2, we list the averaged 65% confidence intervals for distance and inclination. Notice that, while the uncertainties on distance can be extreme, from tens to hundreds of  $mpc$ , the uncertainties on inclination are reasonably small [QUANTIFY THIS WITH CORRECT JACOBIAN]. If it is assumed that a compact object generated GRB maintains bipolar symmetry, the quantity of interest is  $|\cos(\iota)|$ , not  $\iota$ , since observing a compact merger at  $\iota$  and  $\iota + \pi/2$  should produce identical optical counterparts. Since  $|\cos(\iota)|$  maps the bi-modal structure in the inclination PDFs seen in Figure 5 to a single mode, the uncertainties in  $\iota$  will be sufficiently small [QUANTIFY] to provide coincident information on GRB beaming angles.

### 3.3. Sky Localization

Unlike the mass parameters, the recovery of the position on the sky is highly dependent on the location of the source with respect to the detector network in ques-

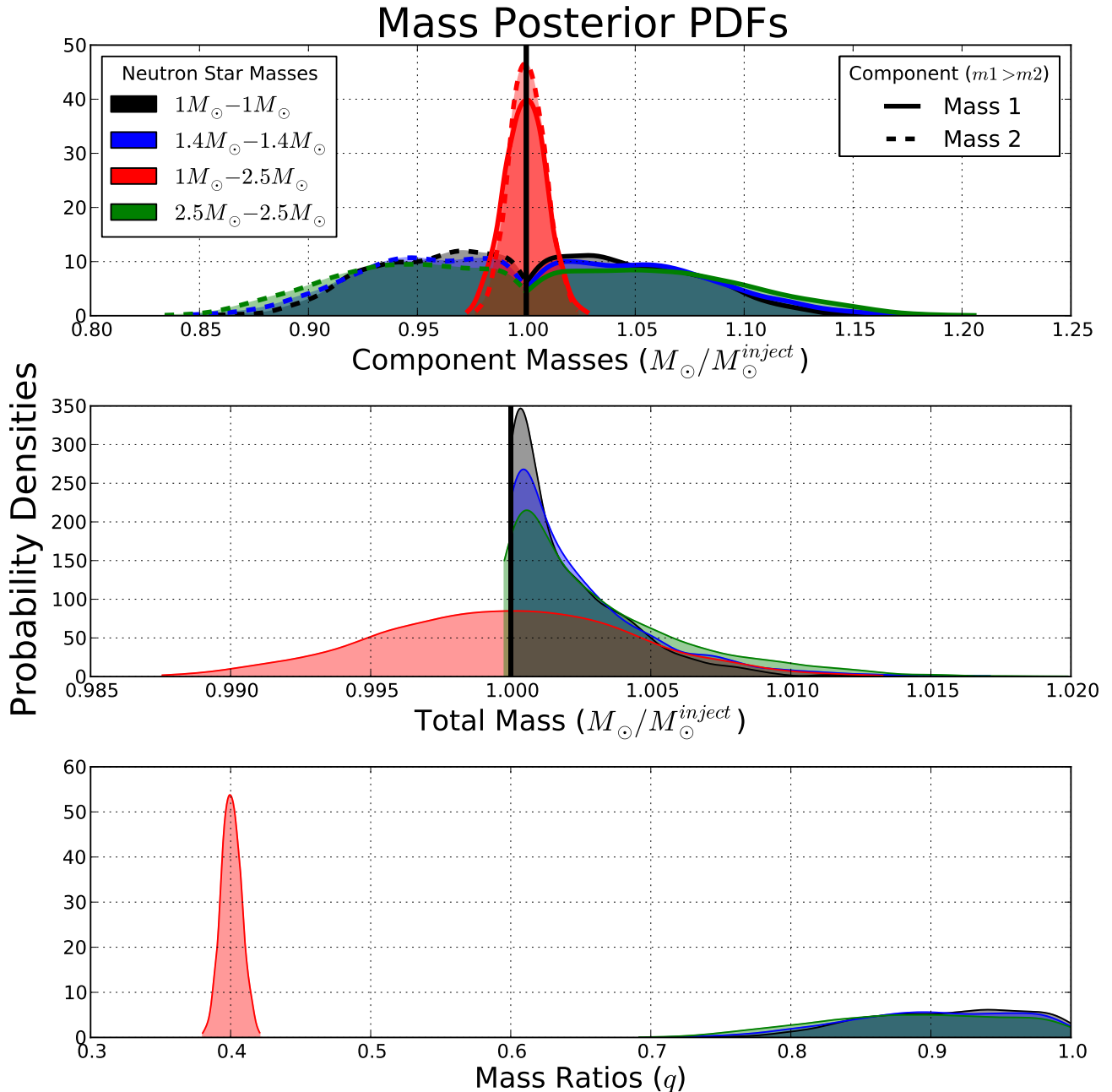


FIG. 4.— Mass PDFs for the four BNS systems, averaged over each of the 40 injections. The average is reported since, in practice, there was quantitatively no difference between the recovered PDFs for different systems with identical masses and SNRs. Systems with identical mass ratios but different total masses have quantitatively identical PDFs when normalized to the true total mass.

tion. For the HLV configuration, the three-detector network can only localize signals to one of two points in the sky. That is, when using only time-of-arrival information, there is equal support in the probability density functions near true location and near the point reflected through the plane formed by the three detectors. See Fairhurst (2011) for a global analysis of time-of-arrival accuracy for various network configurations, including those considered here.

In practice, however, additional information from the wave polarization, can break this plane-reflected degen-

eracy, leading to a bi-modal distribution with significantly more support in one mode of the PDF. By fitting for the sky location and the polarization simultaneously, the MCMC can identify the correct mode on the sky. For the four-detector configuration, this concern is irrelevant: even with time-of-arrival data alone, the HLVI network can constrain any source to a single mode on the sky. Even then, there are still locations on the sky in which two or more detectors are not sensitive to the gravitational-wave signal, distorted, non-Gaussian PDFs.

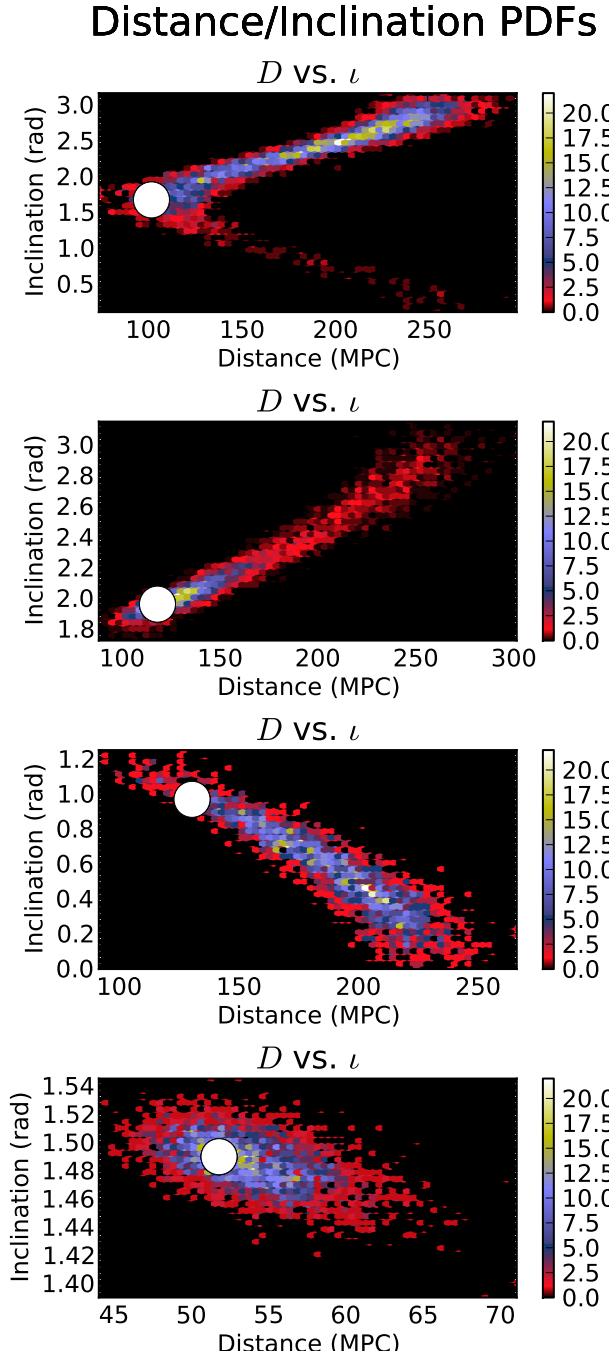


FIG. 5.— Typical marginalized 2D mass PDFs for luminosity distance  $D$  and orbital inclination  $i$ . Notice the bimodal distribution on the first PDF, that can occur when a system is detected nearly “edge-on” ( $i \approx \pi/2$ ). In general, the degeneracy between distance and inclination forces the PDF into one of these two paths when the system is not edge-on, as seen in the second and third PDFs.

The sky location uncertainties for HLV and HLVI are shown in Figures 6 and 7 respectively. We show all four mass bins together, since in practice the mass of the signals has no effect on the recovery of the sky location. Only the location on the sky, the network configuration, and the other extrinsic parameters were found to be rel-

evant. In particular, notice the increase in efficiency between the HLV configuration and the HLVI configuration. In the HLV configuration, there exist points on the sky in which the signal was injected near the plane of the detector network. This causes the elongated, “banana-shaped” PDFs seen in Figure 6. In the HLVI configuration, the plane is no longer relevant, and there are substantially less regions in which only two detectors see a sufficiently strong signal. See Veitch et al. (2012) for a more detailed comparison of the sky-localization benefits of the HLVI configuration versus the three-detector network. As previously, the quantitative results for the two network configurations are reported in Table 2.

#### 3.4. Varied Noise Realizations

We have performed the current analysis on zero-noise injections for two reasons. First, the results of a zero-noise analysis are identical to those that would be achieved by averaging the results of multiple identical injections in different Gaussian noise realizations, as was argued in Section 2.2. The second reason is simply that no good model exists for the true (decidedly non-Gaussian) noise that will arrive with a single detection candidate. Each detection will occur in noisy data, with a specific realization of the PSD provided and with possible instrumentation and environmental glitches. In the case of a unique Gaussian realization of the Advanced-LIGO noise curve, each realization causes the maximum likelihood of the posterior probability distribution to be translated away from the true value; however, these displacements are drawn according to the zero-noise distribution (Rodriguez et al. 2013). Once averaged, the mean uncertainties should be equal to the uncertainty drawn from the zero-noise runs.

As a demonstration of this, we injected a single  $1M_\odot/2.5M_\odot$  system, detected in HLVI, into 5 separate realizations of Gaussian noise colored by the Advanced LIGO PSD, and compared the results to the same MCMC recovery in the zero-noise case. This example can be seen for one-dimensional marginalization of  $\mathcal{M}_c$  and  $q$  in Fig. 8. In effect, the “real answer” that will be recovered is a single PDF with similar width to the zero-noise PDF, but with the peak likelihood displaced from the true value.

Of course, the largest concern for gravitational-wave parameter estimation will not be the specific realization of Gaussian noise, but the effects of glitches in the data. These time-series glitches have a variety of well-known and not-so-well-known physical causes in the instrument, and can cause substantially greater errors in parameter recovery than any specific realization noise realizations. This has already been addressed for the case of space-based gravitational-wave detectors (LISA), and is currently being implemented in `lalinference_mcmc` [TYSON WILL WRITE].

#### 4. CONFIDENCE INTERVALS

When quoting parameter estimation results, it is often convenient to reduce the full parameter space to confidence intervals about single, marginalized parameters. To that end, we state the averaged 65% confidence intervals about the single parameters for each of the three parameter pairs of interest. These were already plotted for the sky locations in Figures 6 and 7.

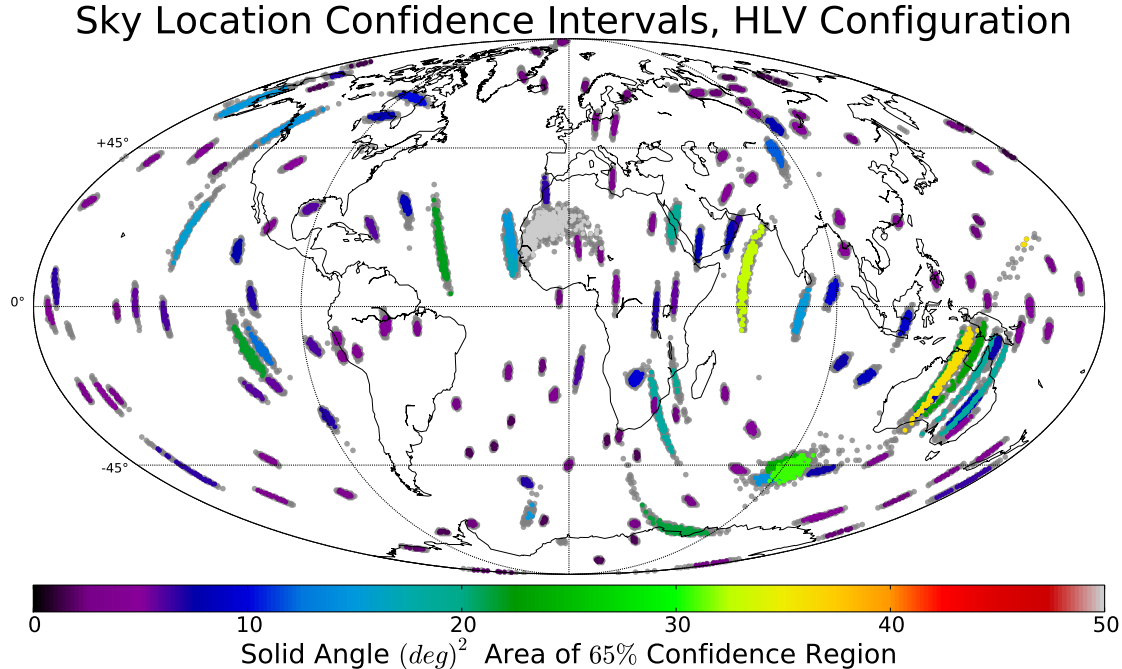


FIG. 6.— The uncertainty on the sky of 160 BNS systems in the HLV detector configuration. Each region represents a single injection, with the colored central region representing the 65% uncertainty region on the sphere, and the gray region representing the 90% uncertainty region. The color scheme indicates the total solid angle size of the 65% region. Note the similar shape of the uncertainty regions at particular points; this is due to the specific realization of our network pattern sensitivity.

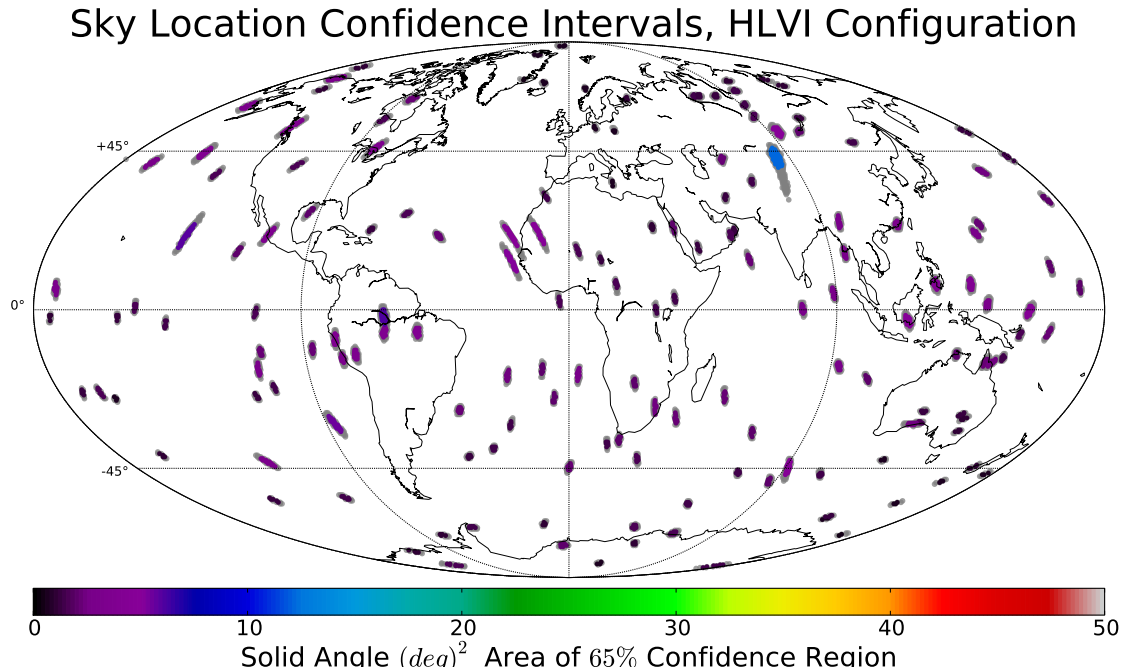


FIG. 7.— The same as Fig 6, except for the HLVI detector configuration. Note the substantially lower average uncertainties on the skies for the majority of the injections. Also note the lack of large, “banana-shaped” uncertainties that were recovered by the HLV configuration. The two improvements are due to the breaking of the degeneracy in sky location recovery that is facilitated by the transition to a four-detector network.

There are several different ways of computing the width of a confidence interval in this setup. If one considers the points in the MCMC as random draws from

the true posterior, then the  $\alpha$ -level confidence interval can be computed by simply ordering the points, removing  $N(1 - \alpha)/2$  points from both sides of the posterior

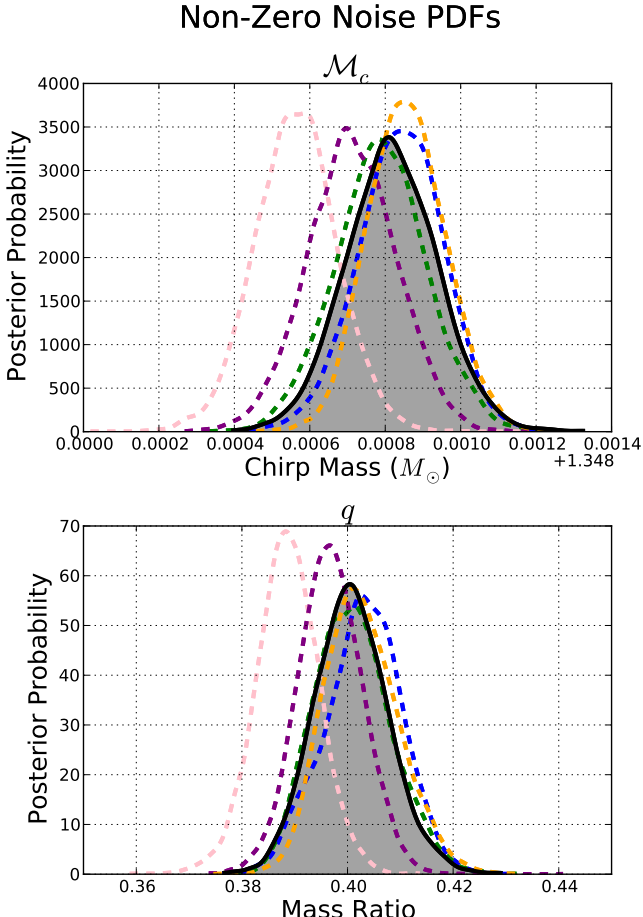


FIG. 8.— The effects of a non-zero noise realization on the recovered PDF for five different Gaussian realizations of the Advanced LIGO noise curve. Each PDF represents the recovery of the same  $1M_\odot/2.5M_\odot$  signal in a different noise curve, picked at random from the Gaussian colored noise defined by the Advanced LIGO power spectral density. Notice how the curve is relatively unchanged, but usually assumes a Gaussian PDF displaced from the true value. This only holds true for glitch-free data, which is an unrealistic idealization when compared to real data.

samples symmetrically, and measuring the width of the remaining points. While this procedure can prove hazardous for multi-modal distributions, it is straightforward and reliable for single-peaked distributions as reported here.

In Table 1, we list the mean 65% confidence intervals recovered for the four mass configurations in both network configurations. This essentially quantifies the widths of the posteriors plotted throughout Section 3. The purpose of Tables 1 and 2 is to provide a quantitative and quotable source for studies seeking to determine how well a physical question about BNS systems can be answered with the Advanced LIGO/Virgo network.

## 5. CONCLUSION

In this paper, we performed an MCMC parameter estimation analysis on the recoverability of basic information about binary neutron stars, using two projected version of the Advanced LIGO/Virgo network. We focused on the recovery of the two masses, the luminosity distance, orbital inclination, and the sky location, as these are the

six basic parameters of physical interest to the problem. We found that, neglecting the effects of spin, the component masses can be constrained to less than 10% of their true value to a confidence of 65%. This value drops below 2% for systems with an asymmetric mass ratio. These results were summarized in Table 1

We also reported on the ability of the two network configurations to constrain the luminosity distance and orbital inclination. For distance, it was found that the uncertainties will fall anywhere from 40 to 100 MPC at 65% confidence, making the uncertainties frequently larger than the luminosity distances themselves. However, it was found that the cosine of the orbital inclination can be constrained to within 0.3 at the 65% level, suggesting that Advanced LIGO/Virgo will be able to offer some information on GRB beaming angles in coincidence with electromagnetic observations.

Finally, we reported the ability of advanced networks to constrain the sky location of BNS signals. It was found that the three-detector configuration, consisting of the Washington and Louisiana LIGO sites plus the Italian Virgo site, was able to constrain all signals within  $60 \text{ deg}^2$  on the sky at the 65% confidence interval, with an average 65% confidence interval of  $\sim 7 \text{ deg}^2$ . Meanwhile, the four-detector configuration, consisting of the three-detector sites plus a LIGO India detector, was able to localize the sky-locations to within  $13 \text{ deg}^2$  on the sky at the 65% confidence interval, with an average 65% confidence interval of  $\sim 2 \text{ deg}^2$ .

It should be noted that there are two distinct types of systematic error, highly relevant to the gravitational-wave parameter estimation problem, that we have not addressed in this study. First, we have studied the parameter estimation uncertainties under the assumption that the waveform template we use to recover the signal template exactly matches the fully relativistic waveforms nature provides. In practice, these waveforms are only approximations to the fully general-relativistic physics required to solve the problem. See [CITE] for a better description of the systematic uncertainties present in the most common waveform families. Additionally, there are several astrophysical assumptions that can potentially contribute to systematic uncertainties in the waveforms, such as the neutron-star equation of state, possible modifications to General Relativity, eccentricity, etc.

Secondly, as stated above, the noise realization that we have employed here is an substantial idealization. In practice the noise levels of Advanced LIGO and Advanced Virgo will be highly variable over time, and will not be stationary or Gaussian, as is commonly assumed. Unfortunately, there is no reliable or simple way to simulate the sort of non-Gaussian detector glitches and instrumentation effects that will arise in any advanced gravitational-wave detector. Since the realization of noise will be the primary factor in the deflection of true signal PDFs from the averages quoted here [TYSON WILL WRITE]

In this study, we have also neglected the effects of spin in the parameter space, electing to focus on the absolute basic parameters that will be measured routinely in the Advanced Detector era. Given the high degree of coupling between the spin and the mass of objects in the gravitational-wave parameter space, it remains unclear if the mass measurement alone will be sufficient to dis-

TABLE 1

MEAN 65% CONFIDENCE INTERVALS FOR INTRINSIC PARAMETERS FOR EACH OF THE FOUR SYSTEMS CONSIDERED. WE REPORT THE CONFIDENCE INTERVALS OF QUANTITIES MEASURED, AS WELL AS THE COMPONENT MASSES AND TOTAL MASS. ALTHOUGH THE RESULTS FOR THE HLV AND HLVI CONFIGURATIONS ARE QUANTITATIVELY IDENTICAL, WE REPORT THEM SEPARATELY FOR CONSISTENCY.

HLVI

System	$\Delta \mathcal{M}_c / \mathcal{M}_c$	$\Delta M_1 / M_1$	$\Delta M_2 / M_2$	$\Delta M_{tot} / M_{tot}$	$\Delta q$
$1M_\odot - 1M_\odot$	$4.70 \times 10^{-5}$	$6.83 \times 10^{-2}$	$6.09 \times 10^{-2}$	$3.67 \times 10^{-3}$	$1.17 \times 10^{-1}$
$1.4M_\odot - 1.4M_\odot$	$8.27 \times 10^{-5}$	$7.27 \times 10^{-2}$	$6.45 \times 10^{-2}$	$4.10 \times 10^{-3}$	$1.24 \times 10^{-1}$
$1M_\odot - 2.5M_\odot$	$1.65 \times 10^{-4}$	$1.74 \times 10^{-2}$	$1.49 \times 10^{-2}$	$8.15 \times 10^{-3}$	$1.29 \times 10^{-2}$
$2.5M_\odot - 2.5M_\odot$	$2.29 \times 10^{-4}$	$8.52 \times 10^{-2}$	$7.41 \times 10^{-2}$	$5.51 \times 10^{-3}$	$1.41 \times 10^{-1}$

HLV

System	$\Delta \mathcal{M}_c / \mathcal{M}_c$	$\Delta M_1 / M_1$	$\Delta M_2 / M_2$	$\Delta M_{tot} / M_{tot}$	$\Delta q$
$1M_\odot - 1M_\odot$	$4.66 \times 10^{-5}$	$6.82 \times 10^{-2}$	$6.09 \times 10^{-2}$	$3.64 \times 10^{-3}$	$1.17 \times 10^{-1}$
$1.4M_\odot - 1.4M_\odot$	$8.31 \times 10^{-5}$	$7.35 \times 10^{-2}$	$6.51 \times 10^{-2}$	$4.18 \times 10^{-3}$	$1.25 \times 10^{-1}$
$1M_\odot - 2.5M_\odot$	$1.65 \times 10^{-4}$	$1.75 \times 10^{-2}$	$1.50 \times 10^{-2}$	$8.19 \times 10^{-3}$	$1.30 \times 10^{-2}$
$2.5M_\odot - 2.5M_\odot$	$2.30 \times 10^{-4}$	$8.53 \times 10^{-2}$	$7.42 \times 10^{-2}$	$5.52 \times 10^{-3}$	$1.41 \times 10^{-1}$

TABLE 2

MEAN 65% CONFIDENCE INTERVALS OF EXTRINSIC PARAMETERS FOR EACH OF THE FOUR SYSTEMS CONSIDERED. AS EXPECTED, THERE EXISTS A SUBSTANTIAL IMPROVEMENT IN THE SKY LOCALIZATION CAPABILITIES OF THE FOUR-DETECTOR HLVI CONFIGURATION OVER THE THREE-DETECTOR HLV CONFIGURATION. NOTE THAT THE SOLID-ANGLE SKY-LOCATION CONFIDENCE INTERVALS,  $\Delta\Omega$ , ARE CALCULATED DIRECTLY ON THE 2D SPHERE, NOT BY COMBINING THE  $\alpha$  AND  $\delta$  UNCERTAINTIES.

HLVI

System	$\Delta D$ (mpc)	$\Delta  \cos(i) $	$\Delta\alpha$ (deg)	$\Delta\delta$ (deg)	$\Delta\Omega$ (deg $^2$ )
$1M_\odot - 1M_\odot$	$3.64 \times 10^1$	$2.23 \times 10^{-1}$	1.45	1.48	1.88
$1.4M_\odot - 1.4M_\odot$	$5.52 \times 10^1$	$2.56 \times 10^{-1}$	1.49	1.50	2.26
$1M_\odot - 2.5M_\odot$	$6.48 \times 10^1$	$2.93 \times 10^{-1}$	1.54	1.64	2.10
$2.5M_\odot - 2.5M_\odot$	$1.06 \times 10^2$	$2.99 \times 10^{-1}$	$1.03 \times 10^1$	1.61	2.22

HLV

System	$\Delta D$ (mpc)	$\Delta  \cos(i) $	$\Delta\alpha$ (deg)	$\Delta\delta$ (deg)	$\Delta\Omega$ (deg $^2$ )
$1M_\odot - 1M_\odot$	$4.34 \times 10^1$	$3.04 \times 10^{-1}$	$1.45 \times 10^1$	6.24	5.57
$1.4M_\odot - 1.4M_\odot$	$5.32 \times 10^1$	$2.87 \times 10^{-1}$	6.92	7.11	8.35
$1M_\odot - 2.5M_\odot$	$6.11 \times 10^1$	$3.11 \times 10^{-1}$	2.67	4.20	7.39
$2.5M_\odot - 2.5M_\odot$	$1.04 \times 10^2$	$3.42 \times 10^{-1}$	$1.13 \times 10^1$	3.31	6.27

tinguish non-spinning neutron stars from highly-spinning low-mass black holes. Future work will explore this potential mass/spin degeneracy, with the aim of definitively answering this question.

## 6. TODO

- Finish adding bibliography/sources
- double check the distribution of sources in Distance/Iota; make sure iota is actually uniform in  $\cos(i)$

## REFERENCES

- Abadie, J., Abbott, B. P., Abbott, R., et al. 2010, The Astrophysical Journal, 715, 14531461, 14531461
- Arun, K. G., Iyer, B. R., Sathyaprakash, B. S., & Sundararajan, P. A. 2005, Phys. Rev. D, 71, 084008, 084008
- Buonanno, A., Iyer, B. R., Ochsner, E., Pan, Y., & Sathyaprakash, B. S. 2009, Phys. Rev. D, 80, 084043, 084043
- Corsi, A., Collaboration, f. t. L. S., & Collaboration, f. t. V. 2012, 8, 8
- Cutler, C., & Flanagan, É. E. 1994, Phys. Rev. D, 49, 2658, 2658
- Fairhurst, S. 2011, Classical and Quantum Gravity, 28, 105021, 105021
- Finn, L. S. 1992, Phys. Rev. D, 46, 5236, 5236
- Gilks, W. R. 1999, Markov Chain Monte Carlo In Practice
- Nakar, E. 2007, Physics Reports, 442, 166236, 166236
- Poisson, E., & Will, C. M. 1995, Phys. Rev. D, 52, 848, 848
- Raymond, V., van der Sluys, M. V., Mandel, I., et al. 2010, Classical and Quantum Gravity, 27, 114009, 114009
- Rodriguez, C. L., Farr, B., Farr, W., & Mandel, I. 2013, arXiv:Working on it...
- Shoemaker, D. 2009, Advanced LIGO anticipated sensitivity curves
- the LIGO Scientific Collaboration, the Virgo Collaboration, Aasi, J., et al. 2013, ArXiv e-prints, arXiv:1304.1775
- Vallisneri, M. 2008, Phys. Rev. D, 77, 042001, 042001
- van der Sluys, M., Mandel, I., Raymond, V., et al. 2009, Classical and Quantum Gravity, 26, 204010, 204010
- van der Sluys, M. V., Röver, C., Stroeer, A., et al. 2008, Astrophys. J. Lett., 688, L61, L61
- Veitch, J., Mandel, I., Aylott, B., et al. 2012, Phys. Rev. D, 85, 104045, 104045